

# INVESTIGATION OF OFFSHORE DC STATION WITH DISTRIBUTED POWER COLLECTION AND CASCADED BOOSTING-VOLTAGE TOPOLOGY: A COMPREHENSIVE STUDY

1.KOLUPAKA HARI KRISHNA, M. TECH (POWER SYSTEMS),

2.N.S. KALYAN CHAKRAVARTHI, PHD, M. TECH.

DEPARTMENT OF ELECTRICAL AND ELECTRONICS ENGINEERING,  
KAKINADA INSTITUTE OF TECHNOLOGICAL SCIENCES, RAMACHANDRAPURAM,  
ANDHRAPRADESH INDIA.

**ABSTRACT:** - In order to collect DC power and boost DC voltage for offshore DC stations, the present research uses a distributed power-collection and cascaded boosting voltage (DPCB) topology made up of several cascaded single active bridges (SABs). In contrast, HVDC stations use the conventional concentrated power-collection and boosting voltage (CPCB) framework. It has high DC voltage boosting powers, is simple to build, is affordable, and offers a low system error rate. The next three variables are looked at. After first determining the DPCB topology with its circuit equations, the phase-shifting control approach is applied to further investigate the operational mechanism. The system minimal signal model is then used to construct a fuzzy control strategy. Third, a fault tolerance strategy with projected power ratio is developed to stop the DPCB station from failing if part of the SABs and generators fail. A significant power differential exists due to windward and wind turbine siting factors. The viability and efficacy of the designed DPCB station with its strategy are finally validated using simulation findings.**INDEX TERMS:** - SAB, fault tolerance, distributed power collecting, cascaded boosting voltage, and topology.

## I. INTRODUCTION

A significant source of renewable energy, offshore wind generating has seen a recent increase in installation capacity [1]. HVDC is more desirable and efficient than HVAC, particularly for offshore wind farms [2]. This study mainly focuses on the topology, mechanism, and strategy for offshore DC converter station under normal operation and fault.

Some AC and DC connected windfarms use the conventional concentrated power-collection and boosting-voltage (CPCB) configuration for offshore DC stations.

In [3], [4], [5], [6], and [7], AC-connected windfarms use a few topologies. A MMC grid-following state-space model is put out in [8] to vividly illustrate the dynamics of the converter in grid-forming mode. For MMC-Based DC Grids, a small-signal stability model is put out in [9] in order to get the best values for the slope coefficients and smoothing reactors. The withstand voltage of the IGBT in Fig. 1 is overridden in [10] by using the modular multilevel converter (MMC) architecture, which has the advantages of low voltage distortion and modular design. To minimise the cost of building the DC station and filter loss, [11] proposes a flexible line commutated converter without an AC filter. In [12], a hybrid DC converter with paralleled MMC and a diode rectifier is suggested to enhance startup capability and performance. However, MMC has a complex structure with several half-bridge or H-bridge submodules (SMs), which requires lots of IGBTs and has a high system cost. Additionally, a large-scale power transformer that is both heavy and bulky is required to boost voltage, which is not advantageous for large-scale offshore station construction and maintenance.

Offshore wind farms connected to DC refer to a few topologies. Due to its benefits of galvanic isolation and bidirectional power flow, the dual active bridge (DAB) is an essential and fundamental converter that is frequently used in medium-voltage DC converters. [13], [14], [15], [16], [17]. [18] proposes a multi-port DC-DC converter topology for MVDC that includes cascading MMC and H-bridges to increase HV bearing capacity and system dependability. To simplify communication and control, [19] proposes an ISOP hybrid conversion architecture based on resonant converters and DAB. A modified DAB dc/dc converter is suggested in [20], which reduces current strains and losses by compensating reactive power using capacitors on the AC side.

To achieve a large voltage gain, a DAB converter with an additional half-bridge circuit is suggested in [21]. [22] describes the development of a DPS control with bidirectional inner phase shifts for DAB to lessen high-frequency transformer current surges and stabilise output power. [23] proposes the use of a multistring step-up resonant converter topology in an MVDC grid to lessen switch voltage stress and loss. [24] proposes an impulse commutated three-phase push-pull topology to improve converter performance and efficiency while lowering system costs.

However, the high-frequency transformer generator converter methods previously stated are not appropriate for offshore DC stations to convert huge amounts of windfarm electricity.

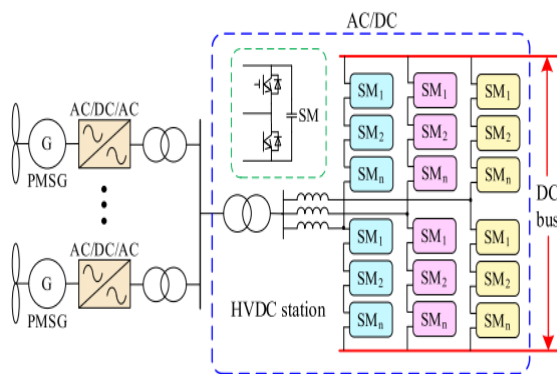


FIGURE 1. CPCB topology structure.

Additionally, certain fault tolerance solutions for MMC and DAB have been widely developed in [25], [26], [27], [28], and [29] to ensure system operation securely because their submodular defects could cause the entire system to fail. A hybrid series converter architecture with a parallel and a series chain link for each phase is suggested in [25] for HVDC in order to achieve a large operating range and DC fault-tolerant capability. A parallel multiple submodule structure is suggested in [26] to enable MMC to operate at high current densities and to filter out high frequency harmonics. [27] proposes a system fault-tolerant configuration as well as a fault detection and localization technique to enhance system robustness and response time for MMC sensor and submodule errors. [28] suggests for an inside-capacitor-energy-storage fault tolerance technique to reduce DC fault current and preserve MMC stability. "Primary-side lower power secondary-side bypass arm" fault-tolerant solution for DAB is proposed in [29] to enhance system load-carrying capacity after fault. In order to increase system dependability, [30] proposes a fault tolerant DAB converter using a central tapped transformer and symmetrical auxiliary inductors. To enhance DC fault ride-

through, [31] proposes an isolated modular multilevel DC-DC converter based on current-fed DAB. However, the bypass submodule or its redundant submodule in the MMC and DAB topological structure is primarily what the fault tolerance systems rely on, which raises the complexity of the structure and the expense of the system.

The advantages of single active bridge (SAB) over double active bridge (DAB) are no cycle power and reduced cost. In [32], [33], [34], and [35], its topology and control approach are discussed. The series connection topology of SAB is suggested in [32] as a means of generating DC electricity for wind farms, although issues related to its mode of operation, the power difference between SABs, and fault tolerance are not thoroughly examined. A fully modular control technique is suggested in [33] to achieve full modular design and enhance system reliability. [34] proposes an indirect I2SOP DC-DC full-bridge converter system that uses asymmetric pulse width modulation to lessen switch voltage stress and the complexity of the filter design. [35] proposes an ISOP converter system to achieve input voltage and output current sharing naturally. The distributed power-collection and cascaded boosting-voltage (DPCB) architecture is used in this research for an offshore DC converter station instead of the typical CPCB topology used in HVDC stations. The primary contributions are as follows.

- 1) A thorough introduction to the structure and benefits of the DPCB is given, along with a comprehensive analysis of how it functions under phase shifting control.
- 2) A tiny signal model is constructed to ensure that the system runs steadily, and PI controllers are created in accordance with the model. Additionally, a Bode diagram is used to analyse system performance.
- 3) DC-voltage target adjustment and predicted power ratio algorithms are proposed to increase system fault tolerance capacity without adding more submodules. Finally, an experiment is used to confirm the viability of the proposed topology and method.

And this is how the document is structured. In Section II, the system topology and operation analysis are explained. Section III provides details on the fault tolerance and system control method. In Section IV, the system experiment is located. In Section V, the conclusions are presented.

## II. SYSTEM TOPOLOGY AND OPERATION ANALYSIS

In contrast to the standard CPCB strategy in Figure 1, a distributed power-collection and cascaded boosting-voltage scheme is used to gather DC power and enhance DC voltage for offshore wind farms. In this section, the DPCB topology is presented along with its benefits and a detailed comparison

to the CPCB topology is made. Additionally, the system equation is derived, and the workings of the system are further examined.

### A. SYSTEM TOPOLOGY STRUCTURE

The DPCB station shown in Fig. 2 is made up of several SABs with a cascaded-connection diode bridge on the secondary side and a noninteractive H-bridge on the primary side. It collects distributed DC energy from a wind turbine and sends high-voltage DC energy to a DC bus. A phase-shifting H-bridge (4-IGBT), a high frequency transformer (T), an input capacitor (CDC), a filter capacitor (C), an inductor (L), and a diode bridge (4-D) make up the SAB.

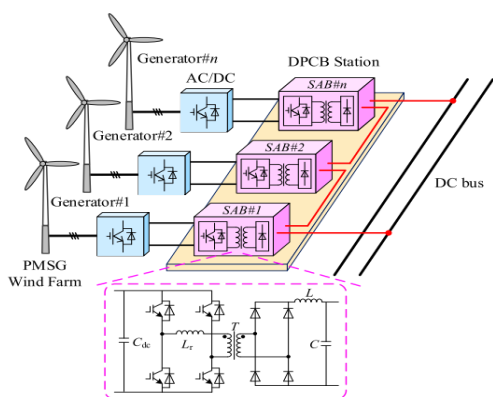


FIGURE 2. The DPCB topology structure.

DPCB stations may have certain advantages to conventional CPCB stations, including the following.

#### 1) Better ability to raise DC voltage

The DC-voltage boosting approach used in DPCB station is stronger and simpler than the method used in CPCB station, which relies primarily on increasing the quantity of cascaded submodular H-bridges and the step-up ratio of the power transformer.

#### 2) Reduced system cost and design difficulty

In order to reduce the quantity of IGBTs and Diodes, the difficulty of the system design, and the expense of the system, SAB is the primary system design without considering cascaded H-bridges at the primary-side, IGBT and Diode withstand voltage, and Circulating Current Restraining.

#### 3) Reduced rate of system errors

Due to each SAB's autonomous operation, submodular malfunction in a non-DPCB station would not result in the complete system failing, proving that DPCB improves system stability.

### B. SYSTEM OPERATION MECHANISM

The system operation mechanism of a DPCB station with three SABs is analysed, and its circuit is depicted in Fig. 3.

To make system analysis easier, Fig. 4's equivalent system circuit, which substitutes an H-bridge, transformer, and Diode-bridge for a regulated voltage source ( $U_{xi}$ ), is used. Except for the current harmonic, each submodule runs separately.

And  $U_{xi}$  is defined by the fixed transformer ratio ( $n$ ) and the transformer's primary-side voltage ( $U_i$ ), which are written as

$$U_{xi} = \begin{cases} nU_i & S1, S4 \text{ or } S2, S3 \text{ on} \\ 0 & S1 \text{ or } S2 \text{ or } S3 \text{ or } S4 \text{ on} \end{cases} \quad (1)$$

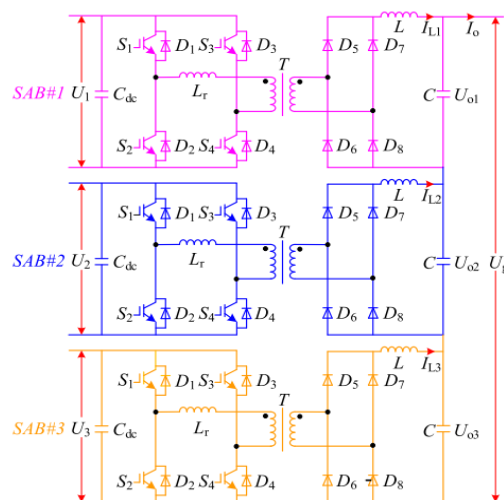


FIGURE 3. DPCB station circuit.

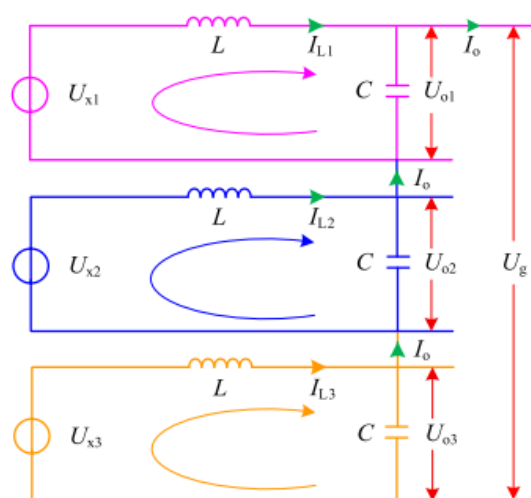


FIGURE 4. Submodular equivalent circuit diagram.

When system loss is considered, the relationship between each SAB's power, voltage, and current is stated as

$$\begin{cases} \{P_{i1} = P_{o1} = U_{o1}I_o \\ \{P_{i2} = P_{o2} = U_{o2}I_o \\ \{P_{i3} = P_{o3} = U_{o3}I_o \quad (2) \\ \{P_o = P_{o1} + P_{o2} + P_{o3} \\ \{U_g = U_{o1} + U_{o2} + U_{o3} \quad (3) \end{cases}$$

$$U_{oi} = \frac{P_{oi}}{\sum_{j=1}^3 P_{oj}} U_g = \frac{P_{oi}}{P_o} U_g \quad i = 1, 2, 3 \quad (4)$$

where  $U_{o1}$ ,  $U_{o2}$ , and  $U_{o3}$  are each SAB's output voltages;  $P_{i1}$ ,  $P_{i2}$ , and  $P_{i3}$  are each SAB's input and output powers;  $P_o$  is the total system power; and  $U_g$  and  $I_o$  are the DC bus voltage and current.

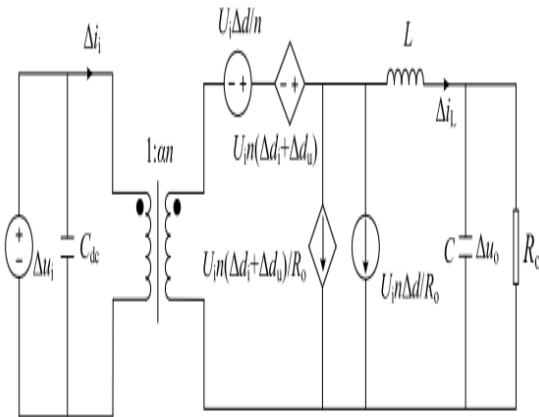


FIGURE 5. DPCB station circuit.

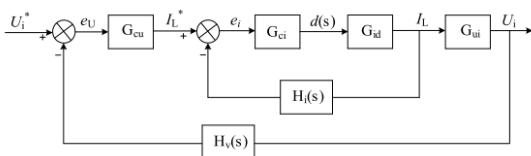


FIGURE 6. Dual cascaded control system diagram.

KVL and KCL state that each SAB equation is provided as

$$\begin{cases} \{I L_i + C \frac{dU_{oi}}{dt} = I_o \\ \{U x_i - L \frac{dI L_i}{dt} = U_{oi} \quad (5) \end{cases}$$

when inductor current ( $I L_i$ ) and output voltage ( $U_{oi}$ ) are concerned.

The link between  $I L_i$  and  $I_o$  is deduced from (5) as

$$I_o = I L_i + C \frac{dU_{oi}}{dt} - C L \frac{d^2 I L_i}{dt^2} \quad (6)$$

The difference between each  $I L_i$  depends on its second derivative and the derivative of  $U_{xi}$ , and each average of  $I L_i$  is equal to  $I_o$ .

Additionally, phase shifting control is used to modify  $U_{oi}$  by altering the phase shifting angle ( $i$ ). And  $i$  is the angle at which the PWM control signals of two diagonal IGBTs (S1, S4) are scattered from one another. The ratio between  $I$  and, known as the phase shifting ratio ( $I$ ), is written as

$$\alpha_i = 1/\pi \phi_i \quad (7)$$

And (8) is the link between  $U_{oi}$ ,  $U_i$ , and  $i$ . Additionally, the phase shifting ratio never reaches 100% and is always constrained within its maximum value ( $\alpha_{max}$ ) due to secondary-side duty-cycle loss.

$$U_{oi} = n \alpha_i U_i \quad (\alpha_i < \alpha_{max}) \quad (8)$$

### III. SYSTEM CONTROL STRATEGY AND FAULT TOLERANCE

The goal of the system control strategy is to maintain system stability and safety during fault and normal operation. Small signal models serve as the foundation for the construction of Fuzzy controllers. Additionally, the impact of power differences on system performance is examined, and a fault tolerance algorithm is developed to increase the system's operational range.

#### A. SYSTEM CONTROL STRATEGY

##### 1) SMALL SIGNAL MODELING

In Fig. 5, a system small signal model of the SAB is created, where  $\Delta d_i$  and  $\Delta d_u$  are duty disturbances brought on by input voltage and output current, respectively, and  $\Delta d$ ,  $\Delta i_L$ ,  $\Delta u_i$  and  $\Delta u_o$  are duty disturbances brought on by input voltage and inductor current, respectively.  $R_o$  is the same as resistance and equals  $R_o = U^2 i / P_i$ .

$\Delta d_i$  and  $\Delta d_u$  are expressed as

$$\begin{cases} \Delta d_u = \frac{4L_T \alpha n^2}{T_s U_i R_o} \Delta u_i \\ \Delta d_i = \frac{4n}{T_s U_i} \Delta i_L \end{cases} \quad (9)$$

A tiny signal model based on KVL and KCL is developed as

$$\begin{cases} \alpha n \Delta u_i + n U_i (\Delta d + \Delta d_u + \Delta d_i) = s L \Delta i_L + \Delta u_o \\ \alpha n (\Delta i_L - s C_{dc} \Delta u_i) = \frac{n U_{in}}{R_o} (\Delta d + \Delta d_u + \Delta d_i) + \Delta i_L \end{cases} \quad (10)$$

From (9) and (10) and under the assumption that  $\Delta u_i = 0$ , the transfer function  $G_{id}(s)$  between  $\Delta d$  and  $\Delta i_L$  is obtained as



$$\beta_i + \beta_j = 1 \quad (15)$$

When the power differential of SABs develops because of the factors of wind turbine location and windward,  $i$  increases with the decreasing of  $j$  but cannot surpass its maximum value  $\max$ . Fig. 8 depicts the variation curve of  $i$  with respect to  $j$ .

And Figure 8 illustrates the relationship between  $i$ ,  $n$ , and  $i$ , where  $i$  varies with  $n$  and  $i$  reaches  $i_{\max}$  when  $i$  reaches  $i_{\max}$ . And the larger  $n$ , the larger  $\max$ , indicating that system may experience a greater power disparity of SABs. When  $n$  changes from  $n_1$  to  $n_2$ ,  $(n_2 - n_1) / n_1$  causes  $\max$  to rise.

Since  $n$  is predetermined during platform building,  $\max$  could no longer be changed online and could only be increased by the target adjustment ( $U_{i^*}$ ), which is designed as follows, when  $\max$  and  $n$  are fixed.

### (2) DC-voltage target adjustment algorithm

When anticipated power ratio ( $\beta_i^P$ ) exceeds its maximum value ( $\max$ ), DC-voltage target ( $U_{i^*}$ ) at the low side is altered and increased by  $\gamma$  in order to increase  $\max$  and lengthen the operational range of the system; otherwise, it retains its original value and is adjusted as shown in Fig. 8.

$$\{U_{i^*} = U_{iN} \beta_i^P \leq \beta_{\max}$$

$$\{U_{i^*} = (1 + \gamma) U_{iN} \beta_i^P > \beta_{\max} \quad (16)$$

The adjusted max power ratio ( $\beta_{\max}$ ) and the difference between  $\max$  and  $\beta_{\max}$  ( $\Delta\beta_{\max}$ ) are calculated from (14) and (16).

$$\{\beta_{\max} = n(1 + \gamma) \alpha_{\max} U_{iN} / U_{gN}$$

$$\{\Delta\beta_{\max} = \beta_{\max} - \beta_{\max} = n\gamma \alpha_{\max} U_{iN} / U_{gN} \quad (17)$$

The process for adjusting the DC voltage goal is shown in Fig. 8 using the example that  $n = n_2 = 2$ . When  $\beta_i^P$  is greater than  $\max$ ,  $U_{i^*}$  is changed from  $U_{iN}$  to  $(1 + \gamma) U_{iN}$ , which causes the maximum power ratio to change from  $\max$  to  $\beta_{\max}$ . As a result, the operating point of  $\beta_i$  instantly changes from A to B. Then, throughout the range from  $\beta_{\max}$  to  $\beta_{\max}$ ,  $\beta_i$  varies along the B-C line. when  $\beta_i$  fluctuates between D and E. And Table 1 lists the values of  $\alpha_{\max}$ ,  $\beta_{\max}$ .

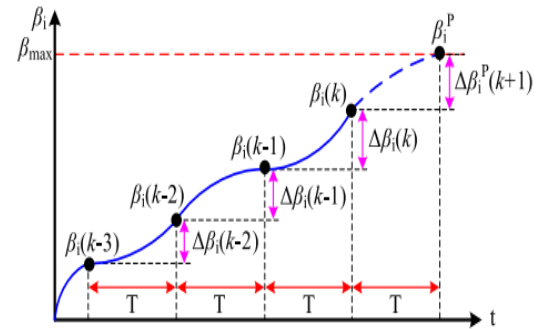


FIGURE 9. Predicted  $\beta_i$  curve.

### (3) Calculating predicted power ratios

The anticipated power ratio ( $\beta_i^P$ ), which is determined from the current power ratio ( $\beta_i(k)$ ) and its changes ( $\Delta\beta_i^P(k+1)$ ) in Fig. 9, is crucial for preventing system breakdown in advance and enhancing its fault tolerance capacity.

$$\beta_i^P = \beta_i(k) + \Delta\beta_i^P(k+1)$$

$$= \beta_i(k) + [Q_1 \Delta\beta_i(k) + Q_2 \Delta\beta_i(k-1) + Q_3 \Delta\beta_i(k-2)] \quad (18)$$

where  $Q_1$ ,  $Q_2$ , and  $Q_3$  are weight factors and  $T$  is the prediction time, and  $\Delta\beta_i(k)$ ,  $\Delta\beta_i(k-1)$  and  $\Delta\beta_i(k-2)$  are the prior power ratio fluctuations, respectively.

### 3) SYSTEM SELF-RECOVERY ABILITY ANALYSIS DURING SUBMODULAR (GENERATOR AND SAB) MALFUNCTION

According to (2) and (4), when a submodule (a generator and SAB) malfunctions, its output voltage  $U_{oi}$  may drop with  $P_i$  and possibly to 0 V, while the output voltages of the other SABs would rise in accordance with (3) with the caveat of (8). The power from rest generators is still generally sent to the DC bus by DPCB DC station without the use of auxiliary submodules, and each low-side DC voltage ( $U_i$ ) could follow its objective by (13). When a submodular malfunction is resolved, the output voltage  $U_{oi}$  may rise along with  $P_i$ , and all system variables may return to their initial states on their own.

## 2 WHOLE CONTROL STRATEGY

Fig. 10 displays the control block diagram for the entire system.

### IV. System setup

A system experimental platform based on ds PACE is constructed, and it comprises of three SABs, a DC bus system, and an imitated DC wind power system. This platform is used to test the viability and efficacy of the DPCB topology and control method (see Fig. 11). A DC battery and

three DC-DC converters with DSP control make up an emulated DC wind power system that produces variable DC electricity. Utilising a programmable DC power supply, a DC bus system is modelled. Tables II shows system parameters and table I shows Fuzzy Rule Box.

To confirm the system's mechanism, operation effectiveness, and fault tolerance capacity, three cases are run.

Case 1: When the system uses its rated power, the operating mechanism is confirmed and examined.

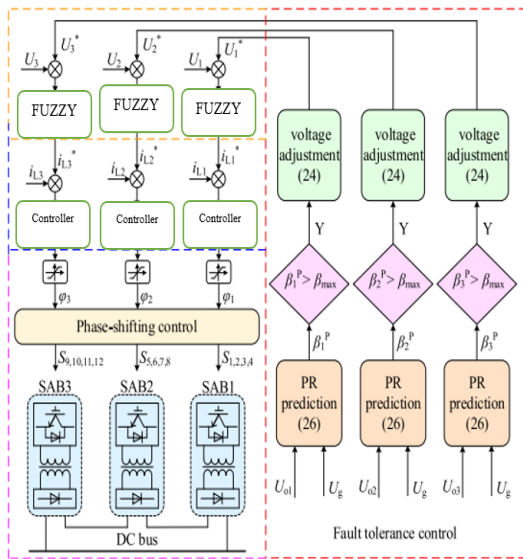


FIGURE 10. Control block diagram of DPCB topology.

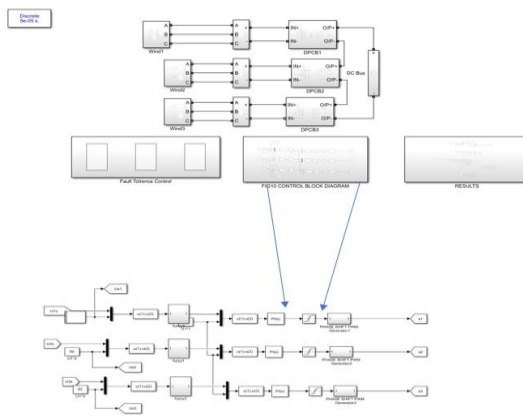


FIGURE 11. System platform.

TABLE II. System parameters.

Symbol	Quantity	Value
$U_{IN}$	Rated low DC voltage	50 V
$U_{gN}$	Rated DC bus voltage	180 V
$P_N$	SAB rated power	500 W
$n$	Transformer ratio	2
$f_s$	Switching frequency	10 kHz
$L_r$	Leakage reactance	56 $\mu$ H
$L$	Filter inductance	153 $\mu$ H
$C$	Filter capacitor	1000 $\mu$ F
$C_{dc}$	Input capacitor	1000 $\mu$ F

Case 2: Input power variation and DC bus voltage fluctuation, which simulate wind power variation and DC bus disturbance, are used to verify, and analyse system steady and transient performance.

Case 3: The ability of the system to tolerate faults is tested and examined when the system malfunctions, simulating instances of generator failure and excessive SAB power difference issues brought on by the placement and orientation of wind turbines.

The findings of the system experiment are depicted in Fig. 12–16, where IL1, IL2, IL3, and Io are represented by the current curves in orange, pink, blue, and purple, respectively. Uo1, Uo2, and Uo3 are represented by the cyan, magenta, and grey voltage curves, respectively; The low DC voltage red, green, and yellow curves correspond to U1, U2, and U3, whereas the black curve represents the voltage target; In addition, the blue, magenta, and cyan power ratio curves in Fig. 12-15 stand for  $\beta_1$ ,  $\beta_2$ , and  $\beta_3$ , respectively. In Figure 16, the blue, green, and cyan curves represent  $\beta P_1$ ,  $\beta P_2$ , and  $\beta P_3$ , while the magenta, red, and black curves stand in for  $\beta_1$ ,  $\beta_2$ , and  $\beta_3$  accordingly.

### A. SYSTEM OPERATIONAL MECHANISM ANALYSIS

Fig. 12 displays the experiment system's results when it is operating at rated power.

In Fig. 12(a), IL1, IL2, IL3, and Io maintain stable values of 7.8 A with errors of 0.15 and 0.05A, respectively; Uo1, Uo2, and U3 maintain stable values of 60 V with an error of 0.001 V; and U1, U2, and U3 track their target of 50 V with an error of around 0.00025 V.

The fluctuation curves of UT1, ILr1, IL1, IC1, and Io for SAB#1 over a control period are shown in Fig. 12(b). The magenta curve (UT1) is 100 V when switch states (S1, S4) change to 1 synchronously. The blue and cyan curves (ILr1, IL1) grow from 0 to 15.9 A and from 7.6 to 7.96 A, respectively. The purple and orange curves (IC1, Io) decline from 0.21 to -0.12 A and from 7.9 to 7.7 A. In 23 s, ILr1 and IL1 fall to 0 and 7.67 A, respectively, whereas IC1 and Io rise

to 0.21 and 7.9 A after 27 s, when S1 switches off and UT1 falls to 0 V. System variations in the next 50 years will be comparable to those in the 50 years prior, except for UT1 and ILr1.

**B. SYSTEM STEADY AND TRANSIENT PERFORMANCE ANALYSIS**

**1) SYSTEM PERFORMANCE ANALYSIS DURING INPUT POWER VARIATION**

When three SAB powers decrease from 525, 500, and 475 W to 500, 475, and 450 W within 0.05s, system results are displayed in Fig. 13.

IL1, IL2, IL3, and Io drop from 7.8 A with errors of 0.11, 0.15, 0.1. Due to the varying current and voltage of each SAB, their current ripples are consistent with (6).

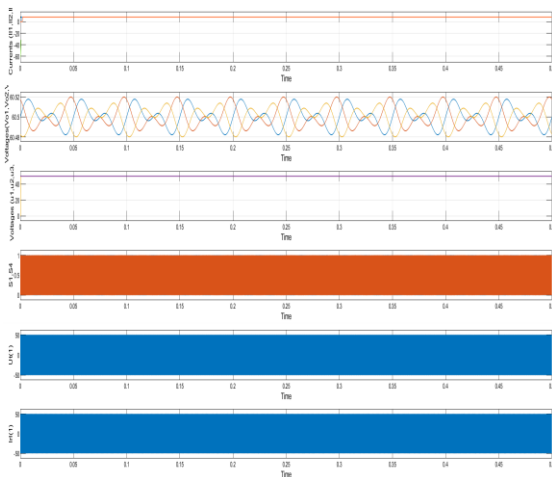


FIGURE 12. The variations of Uo1,2,3, IL1,2,3, Io and U1,2,3, UT1, S1,4.

Each SAB power is related to and consistent with (4) by maintaining Uo1, Uo2, and Uo3 at 63.2, 60, and 56.8 V respectively. With an inaccuracy of just 0.0005 V, U1, U2, and U3 steadily track their goal at 50 V. In keeping with (14),  $\beta_1$ ,  $\beta_2$ , and  $\beta_3$  remain at 0.351, 0.333, and 0.316, respectively.

**2) SYSTEM PERFORMANCE ANALYSIS DURING DC BUS FLUCTUATION**

Figure 14 displays the findings of the experiment system when the DC bus varies from 180 to 189 V, then back to 180V in 0.05 s. Uo1, Uo2, and Uo3 increase by 3.2, 3 and 2.8 V due to their power ratios of 0.351, 0.333, and 0.316 when DC bus voltage abruptly increases by 9 V, whereas IL1, IL2, IL3, and Io fall from 7.8 to 7.5 A within 0.05 s.

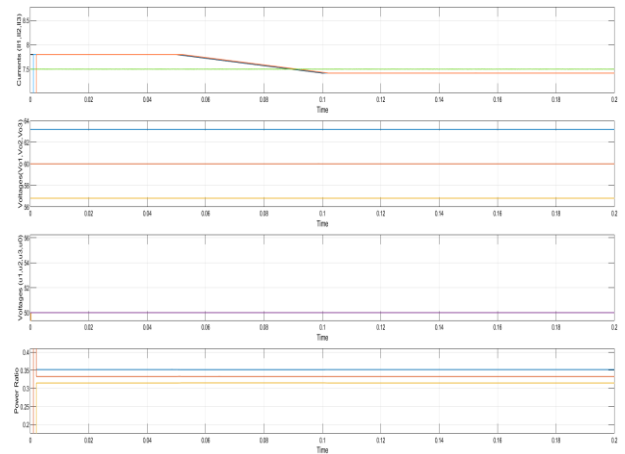


FIGURE 13. The variations of Uo1,2,3, IL1,2,3, Io and U1,2,3 with input power.

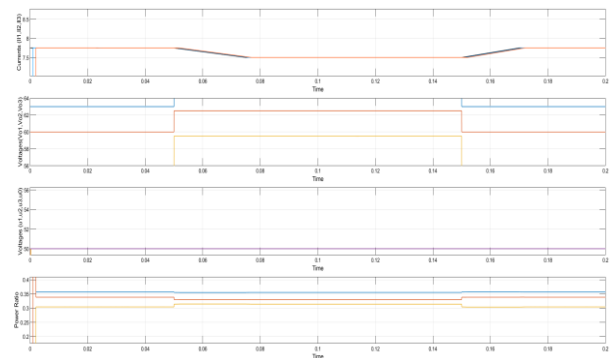


FIGURE 14. The variations of Uo1,2,3, IL1,2,3, Io and U1,2,3 with DC bus voltage.

Normal DC bus voltage rises to 180 V, and after 2.5 Ms, IL1,2,3 and Uo1,2,3 return to their initial levels. In addition, during DC bus fluctuation, U1, U2, and U3 maintain stability at 50 V with maximum errors of 0.001 V. As a result, the system performs well in both steady-state and transient conditions, regardless of changes in input power and DC bus voltage.

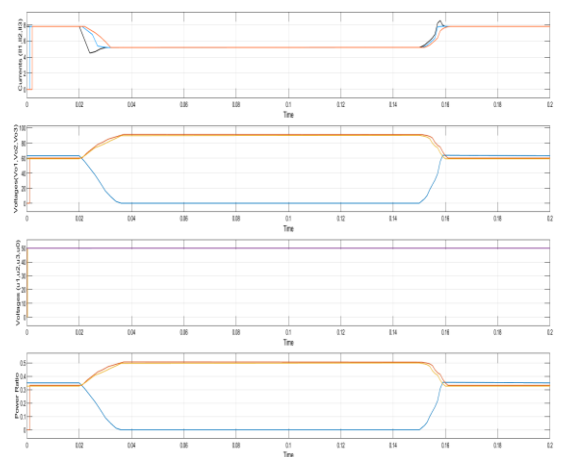


FIGURE 15. The variations of  $U_{o1,2,3}$ ,  $IL_{1,2,3}$ ,  $I_o$  and  $U_{1,2,3}$  with SAB fault.

### C. SYSTEM FAULT TOLERANCE ABILITY ANALYSIS

#### 1.SYSTEM FAULT TOLERANCE ABILITY ANALYSIS FOR GENERATOR MALFUNCTION

Figure 15 displays the results of the experiment system when generator #1 malfunctions and then restarts after 0.2 seconds. When a failure occurs, SAB#1's input power is lost. The values of  $U_{o1}$  and  $I_o$  change from 63 to 0 V and 0.351 to 0, respectively. However, its low-sides DC voltage ( $U_1$ ) continues to steadily track its goal of 50 V. And during 0.15 seconds,  $IL_1$ ,  $IL_2$ ,  $IL_3$ , and  $I_o$  gradually drop from 7.8 to 5.2 A, while  $U_{o2}$  and  $U_{o3}$  rise from 60 to 91.5 V and from 57 to 88.5 V, respectively. As a result,  $\beta_2$ , and  $\beta_3$  shift from 0.333 to 0.51 and from 0.316 to 0.48, respectively, within the confines of a maximum of 0.53.  $U_2$  and  $U_3$  consistently follow their 50 V targets steadily. Within 0.15 seconds of generator #1's recovery, all system variables do the same. These findings are in line with earlier analyses of the system's capacity for self-recovery. As a result, with the max power ratio restriction, the DPCB station performs steadily and continues to supply power from the remaining generators even when a system submodule malfunctions and then recovers.

#### 1) SYSTEM FAULT TOLERANCE ABILITY ANALYSIS FOR EXCESSIVE SAB POWER DIFFERENCE FAULTS

Results for the experiment system are presented in Fig. 16, where SAB#1 power rises quickly in 0.05 s and then returns to its initial value in 0.15 s. The other SAB power ratio falls significantly as SAB#1 power grows quickly.  $\beta_{P1}$ ,  $\beta_{P2}$ , and  $\beta_{P3}$  shift from 0.351, 0.333, and 0.316 to 0.538, 0.235, and 0.224, respectively, and agree with  $\beta_1$ ,  $\beta_2$ , and  $\beta_3$ , which verifies the predicted power ratio algorithm.

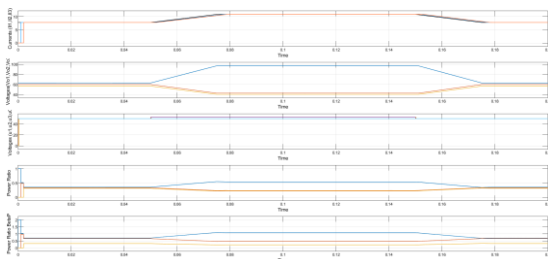


FIGURE 16. The variations of  $U_{o1,2,3}$ ,  $IL_{1,2,3}$ ,  $I_o$  and  $U_{1,2,3}$  when  $\beta_1$  exceeds  $\beta_{max}$ .

$U_{1^*}$  varies between 50 and 52.5 V when  $\beta_{P1}$  exceeds  $\beta_{max}$ , which is consistent with the DC-voltage adjustment method (16). The system continues to function steadily under the suggested fault tolerance technique. Within 0.05 seconds,  $IL_1$ ,  $IL_2$ ,  $IL_3$ , and  $I_o$  go from 7.8 to 10.9 A.  $U_{o1}$ ,  $U_{o2}$ , and

$U_{o3}$  are now 97.1, 42.6, and 40.3 V instead of 63.2, 60, and 56.8 V.  $U_1$ ,  $U_2$ , and  $U_3$  steadily follow their targets. Additionally, all system state variables ( $IL_{1,2,3}$ ,  $I_o$ ,  $U_{o1,2,3}$ ,  $U_{1,2,3}$ ,  $\beta_{P1,2,3}$ ,  $U_{1^*}$ ) change to their original values in 0.005 seconds when SAB#1 power returns to its original value. As a result, the system may function steadily and safely thanks to the proposed fault tolerance and projected power ratio algorithms.

### V. CONCLUSION

Conclusion of the above is as mentioned : The operational mechanism of the system is examined and confirmed for the DPCB topology when the system is running at rated power. When each input generator's power varies and the DC bus voltage fluctuates, Fuzzy controllers built using the system small signal model increase the system's steady and transient performance. The proposed fault tolerance technique improves the system's ability to withstand errors caused by large SAB power differences and submodular malfunction. Further paper can be Implemented using Artificial intelligence Controller like ann or by Using optimization techniques like GA,PSO,Etc..

### REFERENCES

[1] Y. Li, X. Qiao, C. Chen, Y. Tan, W. Tian, Q. Xia, Y. Cao, and K. Y. Lee, "Integrated optimal siting and sizing for VSC-HVDC-link-based offshore wind farms and shunt capacitors," *J. Mod. Power Syst. Clean Energy*, vol. 9, no. 2, pp. 274–284, 2021.

[2] Y. Meng, B. Liu, H. Luo, S. Shang, H. Zhang, and X. Wang, "Control scheme of hexagonal modular multilevel direct converter for offshore wind power integration via fractional frequency transmission system," *J. Mod. Power Syst. Clean Energy*, vol. 6, no. 1, pp. 168–180, Jan. 2018.

[3] S. Wang, L. Zhou, T. Wang, T. Chen, and Y. Wang, "Fast protection strategy for DC transmission lines of MMC-based MT-HVDC grid," *Chin. J. Electra. Eng.*, vol. 7, no. 2, pp. 83–92, Jun. 2021.

[4] X. Li, Z. Li, B. Zhao, C. Lu, Q. Song, Y. Zhou, H. Rao, S. Xu, and Z. Zhu, "HVdc reactor reduction method based on virtual reactor fault current limiting control of MMC," *IEEE Trans. Ind. Electron.*, vol. 67, no. 12, pp. 9991–10000, Dec. 2020.

[5] L. Chen, G. Li, H. Chen, X. Wang, X. Qiao, J. Tang, X. Deng, T. Ding, C. Hong, and J. Yang, "Performance evaluation approach of superconducting fault current limiter

in MMC-HVDC transmission system,” *IEEE Trans. Appl. Supercon.*, vol. 31, no. 8, pp. 1–7, Nov. 2021.

[6] G. Liang and R. Zhu, “Predictive analysis for radiated electromagnetic disturbance in MMC-HVDC valve Hall,” *CPSS Trans. Power Electron. Appl.*, vol. 5, no. 2, pp. 126–134, Jun. 2020.

[7] M. M. Belaunde, M. Ayari, X. Guillaud, and N. B. Bray, “Robust control design of MMC-HVDC systems using multivariable optimal guaranteed cost approach,” *IEEE Trans. Ind. Appl.*, vol. 55, no. 3, pp. 2952–2963, May/Jun. 2019.

[8] G. F. Gontijo, M. K. Bakhsh Zadeh, L. H. Keswick, and R. Teodorescu, “State space modelling of an offshore wind power plant with an MMC-HVDC connection for an eigenvalue-based stability analysis,” *IEEE Access*, vol. 10, pp. 82844–82869, 2022.

[9] H. Li, X. Fan, and S. Liu, “Small-signal stability modelling for MMC-based DC grids with voltage slope control and influence analysis of parameters,” *IEEE Access*, vol. 10, pp. 4686–4698, 2022.

[10] E. Sanchez-Sánchez, D. Grog, E. Prieto-Araujo, F. Dörfler, and O. Gomis-Bellmont, “Optimal multivariable MMC energy-based control for DC voltage regulation in HVDC applications,” *IEEE Trans. Power Del.*, vol. 35, no. 2, pp. 999–1009, Apr. 2020.

[11] Y. Xue, X.-P. Zhang, and C. Yang, “AC filter less flexible LCC HVDC with reduced voltage rating of controllable capacitors,” *IEEE Trans. Power Syst.*, vol. 33, no. 5, pp. 5507–5518, Sep. 2018.

[12] Y. Chang and X. Cai, “Hybrid topology of a diode-rectifier-based HVDC system for offshore wind farms,” *IEEE J. Emerg. Sel. Topics Power Electron.*, vol. 7, no. 3, pp. 2116–2128, Sep. 2019.

[13] Y. Dai, S. Luo, and Z. Li, “Direct power-based control strategy for DAB DC-DC converter with cooperative triple phase shifted modulation,” *IEEE Access*, vol. 9, pp. 147791–147800, 2021.

[14] A. Mustafa and S. Makhila, “Dual phase LLC resonant converter with variable frequency zero circulating current phase-shift modulation for wide input voltage range applications,” *IEEE Trans. Power Electron.*, vol. 36, no. 3, pp. 2793–2807, Mar. 2021.

[15] T. Dai, J. Qin, G. Ge, C. Zhou, L. He, J. Zhai, and J. Li, “Research on transient DC bias analysis and suppression in EPS DAB DC-DC converter,” *IEEE Access*, vol. 8, pp. 61421–61432, 2020.

[16] T.-Q. Duong and S.-J. Choi, “Deadbeat control with bivariate online parameter identification for SPS-modulated DAB converters,” *IEEE Access*, vol. 10, pp. 54079–54090, 2022.

[17] S. Zengin and M. Boztepe, “A novel current modulation method to eliminate low-frequency harmonics in single-stage dual active bridge AC–DC converter,” *IEEE Trans. Ind. Electron.*, vol. 67, no. 2, pp. 1048–1058, Feb. 2020.

[18] G. Sha, Q. Duan, W. Sheng, C. Ma, C. Zhao, Y. Zhang, and J. Tian, “Research on multi-port DC-DC converter based on modular multilevel converter and cascaded h bridges for MVDC applications,” *IEEE Access*, vol. 9, pp. 95006–95022, 2021.

[19] J. Yao, W. Chen, C. Xue, Y. Yuan, and T. Wang, “An ISOP hybrid DC transformer combining multiple SRCs and DAB converters to interconnect MVDC and LVDC distribution networks,” *IEEE Trans. Power Electron.*, vol. 35, no. 11, pp. 11442–11452, Nov. 2020.

[20] A. A. Abou shady, K. H. Ahmed, and I. Abdelsalam, “Modified dual active bridge DC/DC converter with improved efficiency and interoperability in hybrid LCC/VSC HVDC transmission grids,” *IEEE J. Emerg. Sel. Topics Power Electron.*, vol. 9, no. 6, pp. 6963–6973, Dec. 2021.

[21] G. Xu, D. Sha, Y. Xu, and X. Liao, “Hybrid-bridge-based DAB converter with voltage match control for wide voltage conversion gain application,” *IEEE Trans. Power Electron.*, vol. 33, no. 2, pp. 1378–1388, Feb. 2018.

[22] X. Liu, Z. Q. Zhu, D. A. Stone, M. P. Foster, W. Q. Chu, I. Urquhart, and J. Greenough, “Novel dual-phase-shift control with bidirectional inner phase shifts for a dual-active-bridge converter having low surge current and stable power control,” *IEEE Trans. Power Electron.*, vol. 32, no. 5, pp. 4095–4106, May 2017.

[23] M. Abbasi and J. Lam, “A step-up transformer less, ZV–ZCS high-gain DC/DC converter with output voltage regulation using modular step-up resonant cells for DC grid in wind systems,” *IEEE J. Emerg. Sel. Topics Power Electron.*, vol. 5, no. 3, pp. 1102–1121, Sep. 2017.

[24] K. R. Sree and A. K. Rathore, “Analysis and design of impulse-commutated zero-current-switching single-inductor current-fed three-phase push–pull converter,” *IEEE Trans. Ind. Appl.*, vol. 53, no. 2, pp. 1517–1526, Mar. 2017.

[25] S. K. Patro, A. Shukla, and M. B. Ghat, “Hybrid series converter: A DC fault-tolerant HVDC converter with wide operating range,” *IEEE J. Emerg. Sel. Topics Power Electron.*, vol. 9, no. 1, pp. 765–779, Feb. 2021.

- [26] Y. Meng, Y. Zou, H. Wang, Y. Kong, Z. Du, and X. Wang, "Novel submodule topology with large current operation and DC-fault blocking capability for MMC-HVDC," *IEEE Trans. Power Del.*, vol. 36, no. 3, pp. 1542–1551, Jun. 2021.
- [27] R. Picas, J. Zaragoza, J. Pou, and S. Ceballos, "Reliable modular multilevel converter fault detection with redundant voltage sensor," *IEEE Trans. Power Electron.*, vol. 32, no. 1, pp. 39–51, Jan. 2017.
- [28] Y. Xiao and L. Peng, "A novel fault ride-through strategy based on capacitor energy storage inside MMC," *IEEE Trans. Power Electron.*, vol. 35, no. 8, pp. 7960–7971, Aug. 2020.
- [29] N. Zhao, J. Liu, Y. Shi, J. Yang, J. Zhang, and X. You, "Mode analysis and fault-tolerant method of open-circuit fault for a dual active-bridge DC–DC converter," *IEEE Trans. Ind. Electron.*, vol. 67, no. 8, pp. 6916–6926, Aug. 2020.
- [30] H. Shi, H. Wen, G. Chen, Q. Bu, G. Chu, and Y. Zhu, "Multiple-fault-tolerant dual active bridge converter for DC distribution system," *IEEE Trans. Power Electron.*, vol. 37, no. 2, pp. 1748–1760, Feb. 2022.
- [31] Y. Shi and H. Li, "Isolated modular multilevel DC–DC converter with DC fault current control capability based on current-fed dual active bridge for MVDC application," *IEEE Trans. Power Electron.*, vol. 33, no. 3, pp. 2145–2161, Mar. 2018.
- [32] K. Musasa, N. I. Nula, M. N. Gitau, and R. C. Bansal, "Review on DC collection grids for offshore wind farms with high-voltage DC transmission system," *IET Power Electron.*, vol. 10, no. 15, pp. 2104–2115, Dec. 2017.
- [33] W. Chen, X. Jiang, W. Cao, J. Zhao, W. Jiang, and L. Jiang, "A fully modular control strategy for input-series output-parallel (ISOP) inverter system based on positive output-voltage-amplitude gradient," *IEEE Trans. Power Electron.*, vol. 33, no. 4, pp. 2878–2887, Apr. 2018.
- [34] W. Chen, X. Fu, C. Xue, H. Ye, W. A. Syed, L. Shu, G. Ning, and X. Wu, "Indirect input-series output-parallel DC–DC full bridge converter system based on asymmetric pulse width modulation control strategy," *IEEE Trans. Power Electron.*, vol. 34, no. 4, pp. 3164–3177, Apr. 2019.
- [35] F. Liu, G. Zhou, X. Ruan, S. Ji, Q. Zhao, and X. Zhang, "An input-series-output-parallel converter system exhibiting natural input-voltage sharing and output-current sharing," *IEEE Trans. Ind. Electron.*, vol. 68, no. 2, pp. 1166–1177, Feb. 2021.